ADVANCED OPTICAL MATERIALS
www.advopticalmat.de

Space- and Time-resolved Emission Features of Micro- and Nano-sized Perylene-based Zr Metal-Organic Frameworks

Ignacio Romero-Muñiz, José García-Calvo, Carlos Romero-Muñiz, David Rodríguez San-Miguel, Tomás Torres, Félix Zamora,* and Giovanni Bottari**

While many photoresponsive metal–organic frameworks (MOFs) have been reported to date, finding applications in several technologically relevant fields such as photocatalysis, sensors, and light-emitting devices, significantly scarcer are the reports addressing the relationship between the MOFs emissive features and their crystalline domain size (i.e., micro- and nano-sized materials). Herein, a valuable contribution is offered to this issue which consists of the use of reticular chemistry to prepare a Zr-MOF featuring spatially separated tetracarboxylated-functionalized perylenes as ligand. Single crystal X-ray analysis of such Zr-MOF revealed the formation of micro- and meso-porous channels. The perylene-based Zr-MOF exhibited notable opto-electronic features, including a relatively small optical bandgap of 1.82 eV and emission features different from that of the constituting perylene ligand in the solid state. Additionally, local probe techniques are used to unveil the emission properties of isolated Zr-MOF crystals. Space- and time-resolved fluorescence studies revealed a strong dependence of the emissive features of the Zr-MOF, both in terms of its intensity and lifetime, to the crystalline domain size.

1. Introduction

Perylenes are chemically stable polycyclic aromatic hydrocarbons (PAHs) known for their excellent optoelectronic properties such as an intense absorption in the visible region of the solar spectrum and high fluorescence quantum yields (Φ_F).[1–3] These features make them interesting building blocks for their implementation in various light-related technological fields such as organic light-emitting diodes (OLEDs),[4,5] organic photovoltaics (OPVs),[6] and fluorescent markers in biological applications,[7] to mention a few. Due to their planar structure, perylenes also present a strong tendency to π-stack, a process largely exploited, mostly in solution, to promote the formation of supramolecular polymers.[8,9] While such supramolecular polymers frequently present interesting optoelectronic features compared to their molecularly dispersed counterparts, their use in device applications is often hampered by issues related to the reproducibility of their optical properties and processability. In this context, the possibility to incorporate perylene derivatives into large crystalline architectures is highly desirable since it can allow to precisely control the relative arrangement of these chromophores over several length scales thus leading to molecular materials/devices with improved thermal stability and enhanced reproducibility of their optoelectronic features, something which could further

I. Romero-Muñiz, J. García-Calvo, T. Torres, G. Bottari
Departamento de Química Orgánica Facultad de Ciencias
Universidad Autónoma de Madrid
Campus de Cantoblanco
Madrid 28049, Spain
E-mail: tomas.torres@uam.es; giovanni.bottari@uam.es

I. Romero-Muñiz, D. R. San-Miguel, F. Zamora
Departamento de Química Inorgánica Facultad de Ciencias
Universidad Autónoma de Madrid
Campus de Cantoblanco
Madrid 28049, Spain
E-mail: felix.zamora@uam.es

The ORCID identification number(s) for the author(s) of this article can be found under https://doi.org/10.1002/adom.202402127

DOI: 10.1002/adom.202402127

J. García-Calvo, T. Torres, G. Bottari
Institute for Advanced Research in Chemical Sciences (IAdChem)
Universidad Autónoma de Madrid
Campus de Cantoblanco
Madrid 28049, Spain

J. García-Calvo, T. Torres, G. Bottari
IMDEA Nanociencia
C/Faraday 9, Madrid 28049, Spain

C. Romero-Muñiz
Departamento de Física de la Materia Condensada
Universidad de Sevilla
PO Box 1065, Sevilla 41080, Spain

F. Zamora
Condensed Matter Physics Center (IFIMAC)
Universidad Autónoma de Madrid
Campus de Cantoblanco
Madrid 28049, Spain

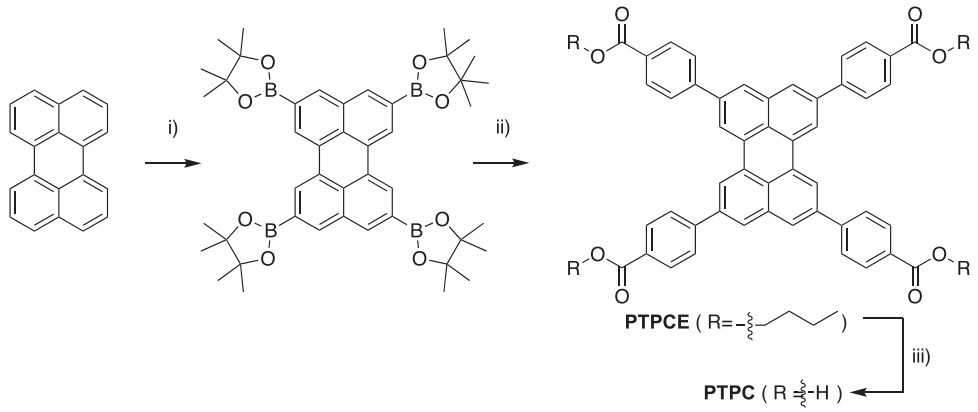

Scheme 1. Synthetic route for the preparation of the **PTPC** ligand. i) $B_2(pin)_2$, $[Ir(COD)OMe]_2$, 4,4′-di-*tert*-butyl-2,2′-bipyridine, cyclohexane, 85 °C, 40 h, 90%; ii) PPh_3, Cs_2CO_3, CsF, $Pd_2(dba)_3$, *n*-butyl-4-yodobenzoate, DMF/THF (1:1), 110 °C, 72 h, 82%; iii) NaOH, MeOH:THF:H_2O (1:1:0.1 v/v/v), 80 °C, 16 h, followed by 1 M HCl addition, 92%. pin = pinacolato; COD = cyclooctadiene; dba = dibenzylideneacetone.

broaden the applicability of these chromophores in technologically relevant fields.

Reticular chemistry is a fast-growing research field that allows to prepare extended network solids featuring a precise and predictable structure from simple molecular building blocks through the formation of covalent or coordinative bonds.[10] Within the class of materials that can be fabricated using reticular chemistry, metal–organic frameworks (MOFs) arguably hold a prominent position. MOFs are well-known porous materials extremely interesting for their chemical diversity and property tunability derived from their modular construction. Especially interesting is the possibility to incorporate chromophores into MOF architectures, enabling precise spatial control of the ligand distribution within the network due to the material's hollow structure.[11–13] Zr-based MOFs incorporating organic[14] or inorganic[15] chromophores are especially interesting materials for their remarkable stability. Such stability can be even further improved through their incorporation in composites,[16–18] broadening the potential applications of the Zr-MOFs.

Up to date, several chromophore-based MOFs have been prepared and successfully used as photoluminescent,[19] photocatalytic,[20] and light harvesting materials.[21] Among the organic chromophores employed, pyrene stands out as one of the most investigated ligand cores.[22] However, surprisingly, scarcer are the MOF reports featuring perylene as a ligand despite the structural similarity, broader chemical versatility, and improved optoelectronic properties of this PAH with respect to its smaller analogue.[23,24]

Herein, we present the synthesis and in-depth characterization of a perylene-based Zr-MOF, namely **Zr-PTPC**, assembled by metal-ligand interactions between tetracarboxylate-substituted perylenes and Zr_6 metal clusters. The structural features of the resulting Zr-MOF were investigated by a wide range of techniques including powder X-ray diffraction (PXRD), N_2 adsorption isotherm, density functional theory (DFT) first principles calculations, Fourier transform infrared spectroscopy (FTIR) analysis, as well as single crystal X-ray diffraction. These studies point out the formation of micro- and meso-porous channels within the Zr-MOF structure which exhibits significant storage capacity and a high surface area. Additionally, the optoelectronic properties of the synthesized Zr-MOF, have been investigated through steady-state fluorescence experiments and complemented by first principles DFT calculations. From these experiments, it could be established that the optical band gap of the perylene ligand is mostly preserved upon its incorporation within the MOF material. Local probe analysis of micro- and nano-sized crystalline samples of **Zr-PTPC** revealed changes in their emission intensity which could be ascribed to the different domain size of the two crystalline Zr-MOFs. A more detailed analysis of the fluorescent lifetime (τ_F) of the different-sized crystals showed a higher contribution of the longer-lived, lower-energy emission components for the smaller domain size material.

2. Results and Discussion

2.1. Synthesis and Structural Characterization of the Zr-PTPC MOF

The synthesis of **PTPC** ligand started with the regioselective preparation of tetrapinacol ester **PTB** which was obtained in 90% yield via the catalytic *ortho*borylation of an unsubstituted perylene with $[Ir(COD)OMe]_2$ (**Scheme 1**). **PTB** was then subjected to a tetra-Suzuki coupling reaction with an excess of *n*-butyl-4-yodobenzoate. The resulting crude was then washed with CH_2Cl_2, yielding tetraester **PTPCE** without the need of column chromatography, increasing the reaction yield from the reported 57% to 82%.[25] Finally, **PTPC** ligand was obtained by saponification of **PTPCE** with NaOH, followed by the acidification of the resulting tetracarboxylate derivative to yield tetracarboxylic acid **PTPC** as a dark red powder in 92%.

Once isolated, **PTPC** was used as a building block for the preparation of a Zr-based MOF. To achieve this goal, pre-formed acetate-based Zr_6 nodes (i.e., $\mathbf{Zr_6O_8H_4(AcO)_{12}}$) were prepared using a methodology reported by Dai et al. (see Experimental Section).[26] A mixture comprising $\mathbf{Zr_6O_8H_4(AcO)_{12}}$ (23 mg), **PTPC** (11 mg), DMF (2 mL), and acetic acid (0.3 mL) as modulator (although other acids such as trifluoroacetic acid could also be used) was then heated at 120 °C for 48 h. The resulting solid was isolated and washed several times with DMF until the supernatant was colorless, followed by washing with water and

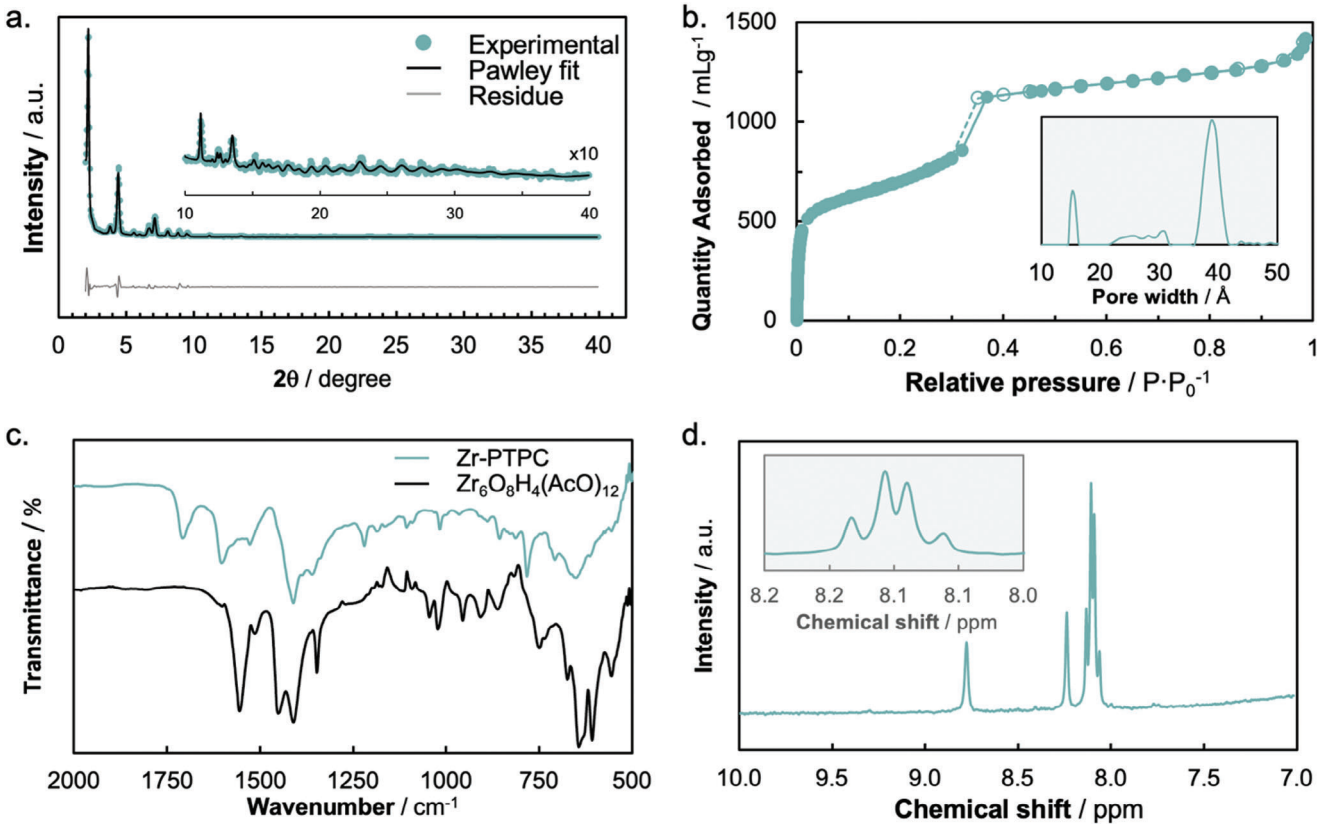

Figure 1. a) Pawley profile refinement of **Zr-PTPC** PXRD data. b) Nitrogen adsorption isotherm of **Zr-PTPC** with an inset of the pores' size distribution. c) FTIR spectra of **Zr-PTPC** (turquoise line) and $\mathbf{Zr_6O_8H_4(AcO)_{12}}$ (black line). d) ^{1}H-NMR spectrum of digested **Zr-PTPC** in DMSO-d_6 (with 3% of D_2SO_4) with an inset of the perylene signals.

acetone, finally yielding the **Zr-PTPC** MOF as a pale orange solid (16 mg).

PXRD analysis of **Zr-PTPC** revealed a phase-pure profile consistent with the *P6/mmm* space group, indicative of a **csq** topology (**Figure** 1a). The lattice parameters were determined through the Pawley refinement of the data, yielding $a = b = 46.0998$ Å and $c = 15.7879$ Å, a structure analogous to the one of NU-1000 MOF[22] with slightly larger cell parameters.

To better evaluate the Zr-MOF's textural properties, a N_2 adsorption isotherm at 77 K was carried out. From such experiment, a two-step profile was observed, the first step occurring in the micropore pressure range and the second ≈0.35 P/P_0, the latter attributed to the mesopores (Figure 1b). **Zr-PTPC** exhibits significant storage capacity with a total pore volume of 1375 $cm^3\ g^{-1}$, of which 1204 $cm^3\ g^{-1}$ is attributed to the micropores which present a Brunauer-Emmett-Teller (BET) surface area of 2492 $m^2\ g^{-1}$. Non-local DFT calculations indicate pores size of 15 and 39 Å, in line with the values calculated from the N_2 adsorption isotherm experiment (inset in Figure 1b) and single crystal X-ray determination (vide infra). These values underscore the potential use of **Zr-PTPC** as storing material of relevant gases for energy storage applications.

FTIR analysis of **Zr-PTPC** revealed characteristic bands attributed to the Zr_6O_8 nodes and the carboxylate linkers, as previously reported in the literature.[27] More specifically, the FTIR spectrum of **Zr-PTPC** displays an intense and broadband ≈650 cm^{-1} associated with Zr node modes, carbonyl symmetric stretching peaks at ≈1360 and 1410 cm^{-1}, carbonyl asymmetric stretching at ≈1530 cm^{-1}, and C=C double bond stretching from the perylene moiety at ≈1707 and 1600 cm^{-1} (Figure 1c; Figure S5.4, Supporting Information). ^{1}H-NMR analysis of the digested MOF clearly shows signals corresponding to the **PTPC** ligand (Figure 1d; Section S9, Supporting Information).

Additionally, periodic DFT calculations on **Zr-PTPC** were conducted to obtain additional insights into the structure of the resulting Zr-MOF. In particular, we employed the VASP 6 code[28] with an energy cutoff of 425 eV for the plane-wave basis set, pseudopotentials built with the projector augmented wave method,[29,30] and the Perdew-Burke-Ernzerhof exchange and correlation functional[31] supplemented by the D3 semi-empirical correction (see further details in the Section S12, Supporting Information).[32] Based on the Pawley refinement, a hexagonal crystal structure belonging to the *P6/mmm* crystal system (space group no. 191) is proposed. The structure comprises an arrangement of $[Zr_6O_8H_4]^{12+}$ clusters "bridged" by **PTPC** units in a 1:2 ratio with each carboxylate group acting as a bidentate ligand. This configuration aligns with the predicted **csq** topology (vide supra), wherein each Zr node functions as an 8-connected center and each organic ligand acts as a 4-connected center. Taking into account the low saturation of the Zr nodes, the DFT model was constructed paying particular attention to the protonation state of the nodes. In this context, various possibilities were

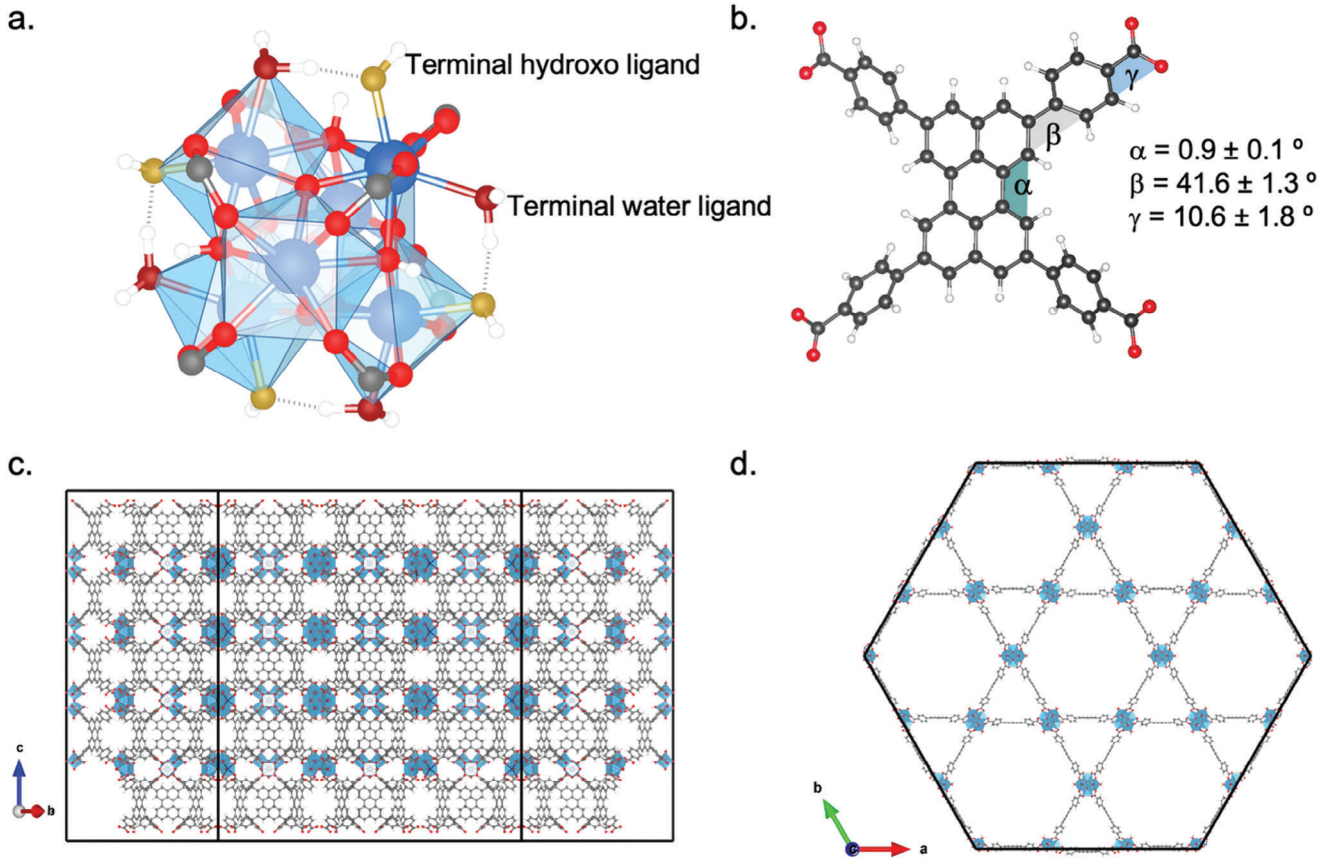

Figure 2. DFT calculated structure of a) the Zr_6 node and b) the **PTPC** ligand within the **Zr-PTPC** MOF. In b), the most representative dihedral angles have been highlighted. Projection of the X-ray crystal structure of **Zr-PTPC** along the c) (11$\bar{2}$0) and d) (0001) planes. Color code: Zr atoms = blue; carbon atoms = black; hydrogen atoms = white; oxygen atoms = red; polyhedra = light blue. In a), for easier visualization of the 3D Zr_6 node geometry, the oxygen atoms of the coordinating water and the hydroxo ligands were highlighted in dark red and yellow, respectively, and one of the six polyhedra has been omitted.

explored using as guidance the reported study on the analogous NU-1000 MOF.[33] For the **Zr-PTPC** model, each Zr_6 metal cluster was coordinated with two carboxylate moieties from two **PTPC** ligands, whereas the remaining eight available sites were saturated by four H_2O molecules and four OH^- hydroxy ligands, alternately inserted to maintain the electrical neutrality of the Zr^{4+} ions (**Figure** 2a). Regarding the arrangement of the **PTPC** ligand within the DFT calculated **Zr-PTPC** model, it can be noticed that the fused benzene rings that constitute the perylene core present a small deviation from planarity (i.e., 0.9 ± 0.1°). On the other hand, a dihedral angle of 41.6° ± 1.3 and 10.6° ± 1.8 was observed between the perylene unit and its adjacent phenyl moieties, and the latter and the carboxylate group, respectively (Figure 2b).

Microsized crystals of **Zr-PTPC** were obtained using conditions similar to those employed to crystallize the NU-1000 MOF (see Experimental Section).[34] X-ray diffraction analysis of the resulting needle-like red crystals pointed out to a *P6/mmm* crystal system, with cell parameters of $a = b = 45.5933$ Å and $c = 15.4727$ Å, and dihedral angles between i) the two perylene halves, ii) the perylene and the phenylene moiety, and iii) the phenylene and the carboxylate moiety of 0°, 42.3°, and 9.4°, respectively (Figure 2c,d). It is worth noticing that these values are close to those obtained by DFT calculations of the **Zr-PTPC** model (i.e., a = 45.7700 Å, b = 45.7965Å, and c = 15.4727 Å).

Scanning electron microscopy (SEM) analysis of nanosized (**Figure** 3a; Figure S8.1, Supporting Information) and microsized (Figure 3b; Figure S8.2, Supporting Information) samples of **Zr-PTPC** revealed the formation of sub-micron structures showing a hexagonal prism morphology but different dimensions: namely, ≈400–500 nm in length and ≈100–200 nm in width for the nanosized crystals and hundreds of μm in length and ≈4 μm in width for the microsized crystals.

Electron dispersive spectroscopy (EDS) analysis on both micro- and nanosized samples showed a relative composition (hydrogen excluded) of C, O, and Zr of 56%, 22%, and 23% (w/w), respectively. This ratio is compatible with the proposed formula unit of $Zr_6C_{96}O_{32}H_{64}$, which has a relative composition of C, O, and Zr of 52%, 23%, and 25% (w/w) (Figure S8.3, Supporting Information).

Considering that the morphology and size of the crystals are features known to influence some of the material properties,[35] additional characterization of the microsized material was conducted to better understand its nature. Most of the characterization techniques, including FT-IR (Figure S5.5, Supporting Information) and PXRD (Figure S3.2, Supporting

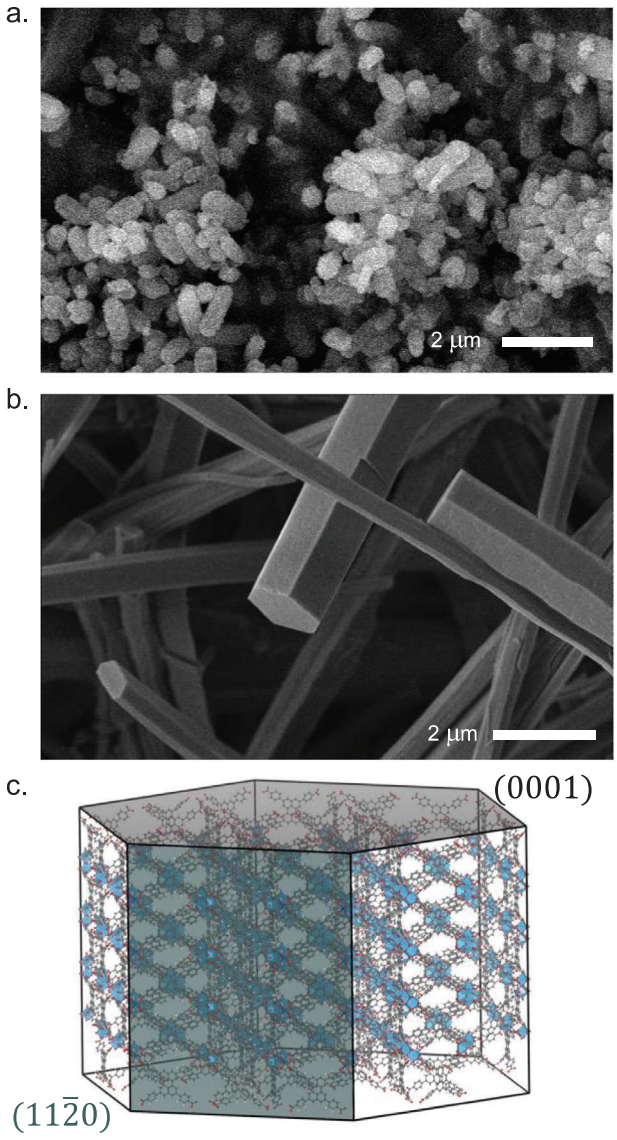

Figure 3. SEM image of a) nanosized and b) microsized **Zr-PTPC** crystalline samples and c) morphological analysis of the crystal facets. For easier visualization of the facets, in c), the (0001) and (11$\bar{2}$0) planes have been shadowed in light grey and light green, respectively.

Information) yielded similar results to those obtained for the nanosized sample. However, slight differences were observed in the N_2 gas adsorption isotherms indicating small variations between the two samples (Figure S6.2, Supporting Information), especially in the calculated external surface area (i.e., 95 m^2 g^{-1} for the microsized sample versus 295 m^2 g^{-1} for the nanosized sample).

2.2. Optoelectronic Properties of the Zr-PTPC MOF

Prior to a detailed investigation of the optoelectronic properties of **Zr-PTPC**, an in-depth photophysical study of the **PTPC** ligand, both in solutions/dispersions and in the solid state, was performed. For interpreting these latter experiments, it is important to take into account that, due to their planar structure, perylenes present a strong tendency to aggregate (vide supra), a phenomenon which in turn strongly affects the molecules emission features.[36] For instance, while unsubstituted perylene dissolved in cyclohexane emits at 436 nm, such emission experiences a significant red shift (i.e., > 150 nm) upon forming crystalline structures.[37] Aggregation of perylene derivatives in solution can also lead to important variations of the chromophore emission with respect to the molecularly dispersed species as a result of the different spatial disposition and angles between the interacting chromophores giving rise to either a red-shifted or blue-shifted emission upon forming *J*- or *H*-aggregates, respectively.[38]

The absorption spectrum of **PTPC** in DMF, a solvent in which the ligand is perfectly soluble at the investigated concentration (i.e., 5×10^{-6} M), showed three sharp and intense bands maximizing at 402, 426, and 454 nm (Figure S10.1a, Supporting Information). On the other hand, in water, a solvent in which **PTPC** forms dispersions, the ligand showed a broad and featureless absorption spectrum spanning from 350 to 560 nm (Figure S10.1b, Supporting Information). Despite the striking differences in the absorption features of **PTPC** in DMF and water, the emission spectra of the ligand in the two solvents were similar in the 430–545 nm region, both showing three intense bands ≈462, 491, and 527 nm (Figure S10.1, Supporting Information) (deconvoluted spectra in Figure S10.3, Supporting Information and deconvoluted peaks in Table S10.1, Supporting Information). However, in water, an additional broad band peaking at 591 nm and spanning from 550 to 700 nm was observed. In perylene derivatives, such low-energy transition is typically attributed to the emission of the excimers.[39] Turning to the solid-state optical characterization of the **PTPC** ligand, a broad excitation spectrum was observed showing intense transitions between 350 and 610 nm (**Figure** 4a, green line). A broad spectrum spanning from 450 until 750 nm was also recorded in the case of the emission features of the ligand in the solid state (Figure 4a, black line), which was deconvoluted in four Gaussian components (Figure 4c). The three deconvoluted higher-energy components (i.e., λ_{em} = 462, 490, and 521 nm, Table S10.2, Supporting Information) which combined have a small contribution to the overall emission (i.e., < 3%), exhibited shapes and positions consistent with the emission of **PTPC** in DMF (Figure S10.1, Supporting Information). Additionally, a large deconvoluted band, contributing up to 97% to the overall emission, was seen maximizing at ca. 600 nm. Taking into account that this value is close to that observed for the ligand dispersed in water (vide supra), it is reasonable to attribute it to the emission of perylene aggregates in the solid state. The solid-state Φ_F of **PTPC** was also determined, obtaining a value of 10% which is significantly lower than that of the ligand molecularly dissolved in DFM (i.e., 85%).

Next, the solid-state emissive features of nanosized **Zr-PTPC** samples were recorded (Figure 4d, black line). For this MOF, a blue-shift of the emission maximum ($\lambda_{em.}$ maximum = 567 nm) accompanied by an overall broadening of the emission band was observed compared to **PTPC** in the solid state. In contrast, microsized **Zr-PTPC** samples showed a red-shifted emission with respect to the nanosized material, with an intensity maximum at 700 nm (Figure S10.6, Supporting Information). Deconvolution of the broad emission band in nanosized **Zr-PTPC** points

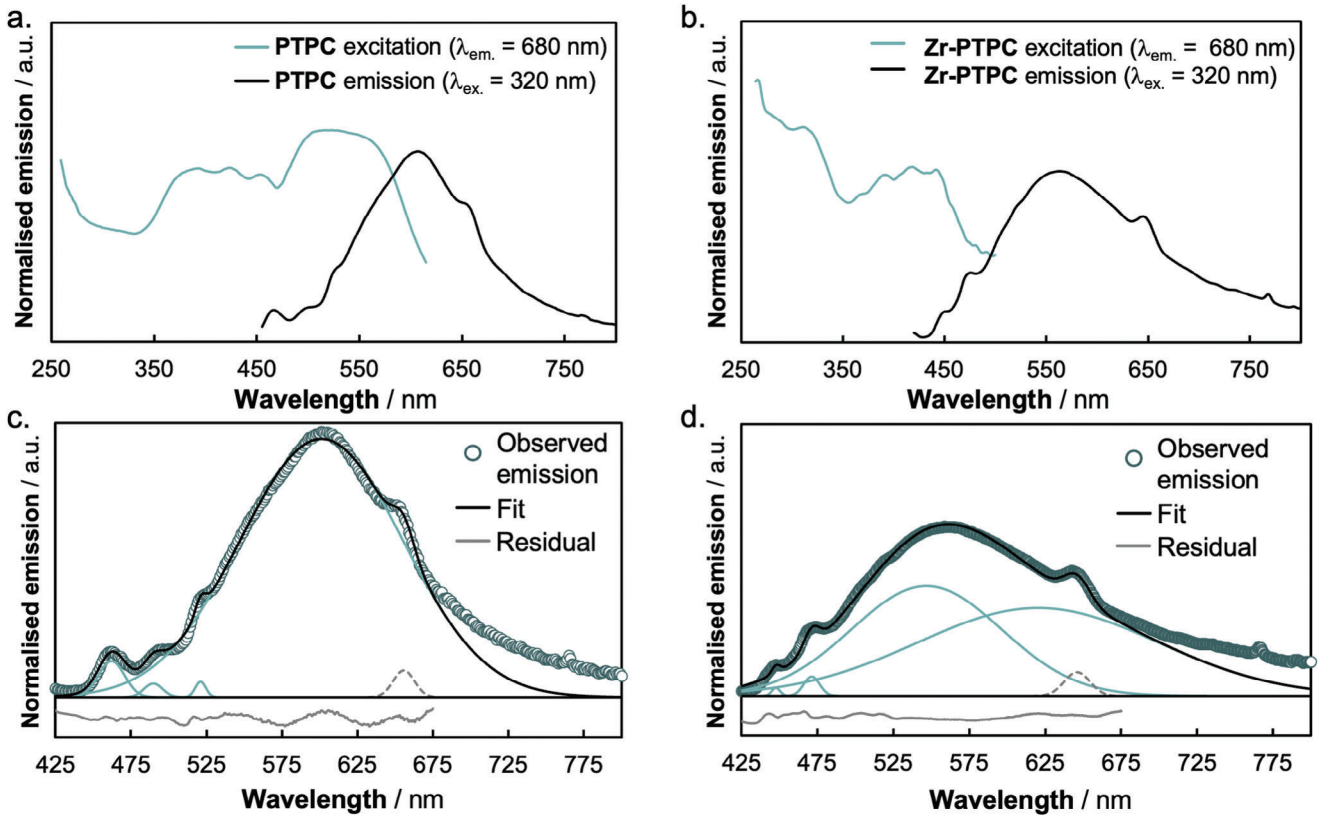

Figure 4. Solid-state excitation and emission spectra of a) **PTPC** ligand and b) nanosized **Zr-PTPC** samples. Deconvolution (light green lines) of the solid-state emission spectra of c) **PTPC** ligand and d) nanosized **Zr-PTPC**. In c) and d), deconvoluted dashed grey line components at 646 nm are due to the first harmonic of the excitation.

out four main contributions, two of which, centered at 547 and 620 nm, accounted together for > 99% of the MOF emission (Figure 4d). On the other hand, the lower energy electronic transitions in both Zr-MOFs are most probably originating from perylene/perylene excited state interactions, moieties which the crystalline nature of **Zr-PTPC** maintain fixed at a short distance within the small triangular pores (e.g., perylene-perylene center-to-center distance ~12 Å) (Figure 2d). Interestingly, a similar trend was previously observed for a Ce-MOF comprising a tetrabenzoate pyrene ligand.[40] The observed differences in emission maxima between the nano- and the microsized **Zr-PTPC** suggest the presence of perylene/perylene interactions of different nature and/or relative contribution in both Zr-MOF materials. Additionally, Φ_F of 2.5 and 1.8% were determined for the nanosized and microsized **Zr-PTPC**, respectively, which represents more than a four-fold decrease with respect to the value recorded for **PTPC** in the solid state (vide supra) ascribable to an effect related to the inclusion of the ligand within the MOF architecture. A similar trend (i.e., lower Φ_F for the MOF with respect to the ligand), was previously observed in some pyrene-based MOFs.[41]

Absorptance measurements of the nanosized **Zr-PTPC** were also performed (**Figure 5a**). The resulting spectrum, which matches the recorded excitation spectrum (vide supra), allowed to calculate, by using a Tauc plot, the optical band gap of the MOF material which is 1.82 eV (Figure 5b). This value is close to that recorded for **PTPC** in the solid-state (i.e., 1.79 eV, Figure S10.10, Supporting Information). Calculations of the density of states (DOS) of the **Zr-PTPC** MOF afforded a calculated band gap of the MOF material of ≈1.80 eV, in line with the value observed for the optical band gap, while evidencing a strong contribution of the perylene moiety around the Fermi level (Figure 5c). This finding substantiates the relevant contribution of the perylene ligand to the overall absorption properties of the **Zr-PTPC** MOF.

Next, local probe techniques such as confocal fluorescence microscopy and fluorescence lifetime imaging microscopy (FLIM) were used to investigate the space- and time-resolved emission features of **Zr-PTPC** as a function of the Zr-MOF crystalline material domain-size (i.e., nanosized versus microsized). First, confocal fluorescence microscopy ($\lambda_{ex.}$ = 454 nm) experiments of nano- and micro-sized **Zr-PTPC** crystalline samples, as well as powder samples of the **PTPC** ligand, were carried out recording the emission across two different spectral regions (i.e., 480–580 and 600–700 nm) (**Figure 6a**). The two selected optical windows were chosen to pinpoint emissions mainly stemming from *intra*perylene $S_1 \rightarrow S_0$ (i.e., higher energy spectral region) and *inter*perylene, aggregate-mediated deactivation channels (i.e., lower energy spectral region),[41,42] with the ultimate goal of underpinning possible effects of the Zr-MOF crystalline domain size on the material emission features.[40]

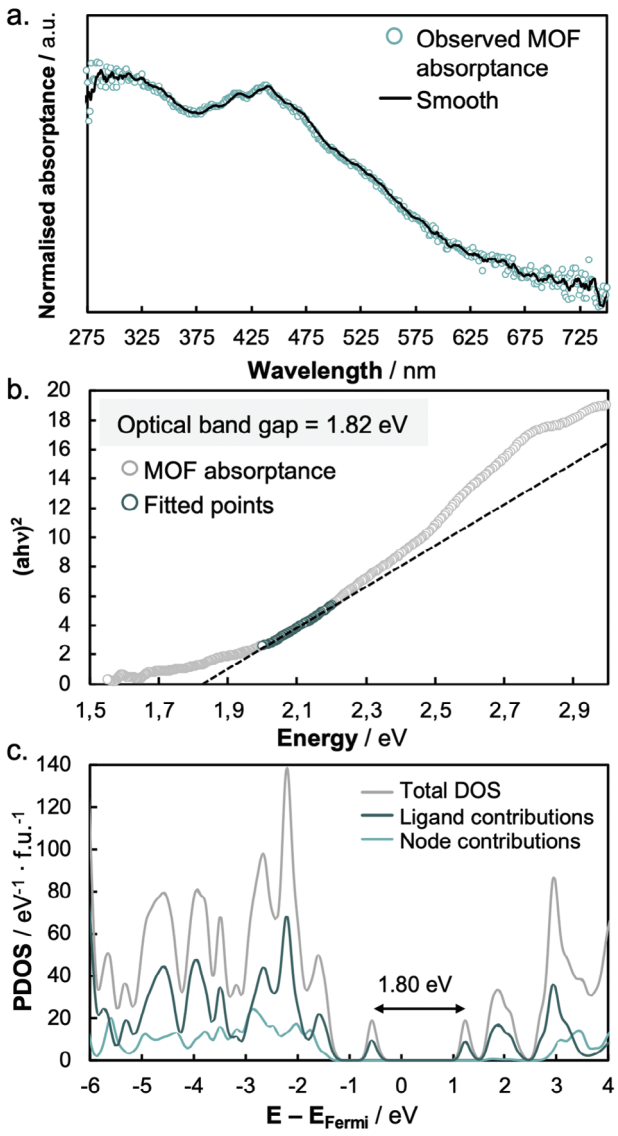

Figure 5. a) Absorptance spectrum of **Zr-PTPC**. b) Tauc plot of the **Zr-PTPC** MOF absorptance with the fitted points (dashed straight line) highlighted in green. c) Calculated density of states of **Zr-PTPC** (grey line), and projected DOS from the **PTPC** ligand (dark green line) and the Zr_6 node (light green line). A double arrowed horizontal line in c) indicates the optical band gap in **Zr-PTPC**.

On the one hand, confocal microscopy studies on the nanosized **Zr-PTPC** crystalline material showed, for the two investigated spectral windows, images of comparable relative emission intensity (Figure 6c). A similar behavior was also observed in the case of the **PTPC** ligand (Figure S11.1, Supporting Information). On the other hand, when microsized **Zr-PTPC** crystalline samples were imaged, it was observed that crystals with a high aspect ratio (Figure 6d, red dashed square) appeared significantly more emissive in the 600–700 nm interval window (Figure 6d, right hand-side) than in the 480–580 nm one (Figure 6d, left hand-side). Considering that the chemical composition of the nano- and micro-sized **Zr-PTPC** is identical, an explanation for the dissimilar emission response observed in confocal microscopy as well as bulk measurements (vide supra) for the two crystalline materials could be ascribed to their different domain size. Such morphological feature could influence the relative contribution of the *inter*perylene radiative deactivation transitions (e.g., *intra*crystal interactions between perylene moieties within the Zr-MOF smaller pores and *inter*crystal interactions between "contacted" crystals).

To gain further insight into the domain size-dependent emission features of nano- and micro-sized crystalline samples of **Zr-PTPC**, FLIM was used which combines local probe microscopy imaging with τ_F measurements to visualize domains of a given sample as a function of τ_F. In this context, one should take into account that perylenes are reported to have a solid-state *inter*perylene τ_F ranging from 1.9 up to 20 ns, with the higher value mainly related to spatial interactions of perylenes in their aggregated form.[43,44] Amplitude average fluorescence lifetime (τ_{av}) measurements on **Zr-PTPC** showed, in the 600–700 nm spectral region, shorter values for the microsized sample with respect to the nanosized one (i.e., 0.23 vs 0.37 ns) (Table S11.1, Supporting Information), a result which suggests a higher contribution of longer-lived radiation processes in the latter material (i.e., *inter*perylene interactions). Interestingly, while the microsized ribbons exhibited uniformly short τ_{av} values along their entire length (Figure 6b; Figures S11.5, and S11.6, Supporting Information), longer τ_{av} values were observed in the regions where two single crystals are in contact (see dashed square region in Figure 6b). Such τ_{av} increase can be attributed to a higher contribution, in the "contacted" region, of *inter*crystal interactions between perylene moieties exposed at the crystal facets (see Figure 3c).

A more detailed analysis of the Zr-MOF emission features of micro- and nanocrystalline samples in the 600–700 nm spectral region was performed by deconvoluting τ_{av}. As in the case of similar studies carried out on pyrene-based MOFs,[37,40,43] the τ_{av} of **Zr-PTPC** was deconvoluted into three components (i.e., τ_1, τ_2, and τ_3) (Table S11.1, Supporting Information). Looking at the longer lasting τ_3 components, higher values were seen for the nanosized crystalline samples with respect to the microsized ones (i.e., 3.1 vs 2.2 ns) (Table S11.1, Supporting Information), a result which can be attributed to a higher contribution of *inter*crystal perylene interactions in the former sample. On the other hand, in the microsized crystals, the relative contribution of the *intra*crystal perylene interactions increases thus leading to shorter τ_3 values. To further validate this hypothesis, microsized crystals were mechanically grounded as a way to increase the *inter*crystal perylene interactions. The resulting grounded **Zr-PTPC** sample yielded a τ_3 value of 2.5 ns, indicating that enhanced *inter*crystal perylene interactions contribute to the observed increase in τ_3, thus corroborating the proposed hypothesis regarding the influence of crystalline domain size on the Zr-MOF emission properties.

These findings underscore the potential application of the fabricated nanosized and microsized perylene-based Zr-MOFs in sensors, diagnostics, and devices, as their tunable emission properties, driven by controlled *inter*- and *intra*crystalline interactions, offer tailored emission ranges and fluorescence lifetimes, making them interesting candidates for advanced optical and electronic applications.

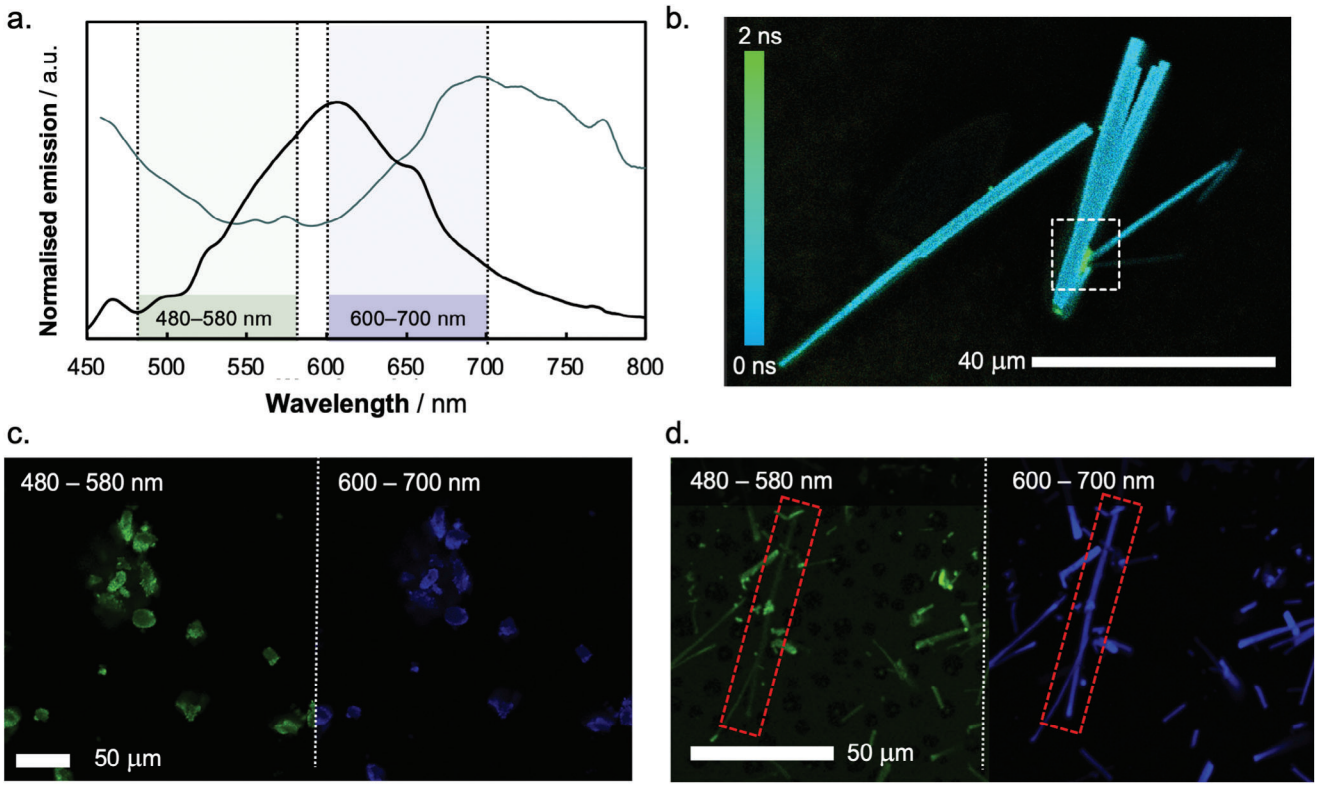

Figure 6. Solid-state emission spectra of a) a nanosized (black line) and b) a microsized (green line) **Zr-PTPC** crystalline sample. The two spectral regions probed in the confocal fluorescence microscopy and FLIM experiments have been highlighted in light green (i.e., 480–580 nm) and light blue (i.e., 600–700 nm). b) FLIM image of a few microsized **Zr-PTPC** crystals probed in the 480–700 nm region. A dashed white square indicates an overlapping region between two crystals. Confocal fluorescence images (λ_{ex} = 454 nm) of the same region for c) nanosized and d) microsized **Zr-PTPC** crystalline samples collecting emissions in the 480–580 (left hand-side) and 600–700 nm spectral interval (right hand-side). In c) and d), the same bright adjustment has been applied. In d), a dashed red box has been included to help visualizing the different emission intensities of a microsized rod-like crystal in the two investigated spectral regions.

3. Conclusion

Herein, we report the preparation of a perylene-based Zr-MOF (**Zr-PTPC**) assembled by metal-ligand interactions between a tetracarboxylate-functionalized perylene ligand (**PTPC**) and Zr_6 metal clusters. The precise 3D arrangement of the ligand and the cluster within the Zr-MOF material was determined by single crystal X-ray analysis revealing the formation of micro- and meso-porous channels which confer to the MOF a high surface area and a significant storage capacity. The optoelectronic properties of **Zr-PTPC** have been investigated by using a wide range of spectroscopic and microscopic techniques and compared to those of the **PTPC** ligand in the solid state. Interestingly, similar optical bandgaps were determined for the **Zr-PTPC** MOF and the **PTPC** ligand in the solid-state (i.e., 1.82 and 1.79 eV, respectively), in contrary to what is commonly observed in Zr-MOFs which mostly act insulators. DFT calculations helped to explain such result by evidencing a strong contribution of the perylene moiety around the Fermi level in the **Zr-PTPC** architecture. On the other hand, a dissimilar behavior in the solid-state emission features of **Zr-PTPC** and **PTPC** was observed, with the Zr-MOF material presenting a broader spectrum with respect to the free ligand. Moreover, clear differences in the emission intensity of micro- and nano-sized crystalline samples of **Zr-PTPC** were observed depending on the investigated spectral region (i.e., 480–580 and 600–700 nm, optical windows mainly related to *intra*perylene $S_1 \rightarrow S_0$ and *inter*perylene, aggregate-mediated deactivation transitions, respectively), a phenomenon which could be ascribed to the different domain size of the two crystalline MOF materials. Finally, FLIM measurements of the Zr-MOF emission features of micro- and nano-sized crystalline samples in the 600–700 nm spectral region were carried out. These studies revealed a higher contribution of the longer-lived, lower-energy emission components in the nanosized material with respect to the microsized sample, a result attributable to a higher contribution of the *inter*crystalline interactions in the nanosized crystalline Zr-MOF sample. We are currently carrying out advanced spectroscopic studies aiming to underpin the nature of the emissive properties of **Zr-PTPC** samples in bulk.

We reckon that the present work adds a valuable contribution to the field of local probe emission studies on photoresponsive MOFs as a function of their domain size, an issue poorly explored. Moreover, structural modification of the reported Zr-MOF by functionalization of the perylene unit at its *peri* and/or bay regions with electroactive moieties and/or different anchoring groups could allow to prepare perylene-based Zr-MOFs analogues of **Zr-PTPC** showing tuneable optoelectronic

properties, a research line that we are currently investigating in our laboratories.

4. Experimental Section

Synthesis of **PTPC** ligand. PTPCE (320 mg, 0.33 mmol) and NaOH (242 mg, 6 mmol) were dispersed in a mixture MeOH/THF/H_2O (32/32:3.2 mL) and heated at 80 °C overnight. Once the mixture did not show the presence of starting material by TLC, the reaction was stopped, cooled down to room temperature and the solvents evaporated under vacuum. Then water (100 mL) and NaOH (200 mg) were added. After stirring for 1 h at room temperature, the dispersion was filtered, and the filtrate acidified with HCl 1 M observing the formation of a red precipitate that was collected by centrifugation and dried overnight under vacuum affording **PTPC** ligand as a dark red solid powder (222 mg, 92% yield). ^{1}H-NMR (300 MHz, DMSO-d_6): 8.82 (s, 4H, CH), 8.25 (s, 4H, CH), 8.06 (s, 8H, CH).

Synthesis of $Zr_6O_8H_4(AcO)_{12}$. The synthesis of Zr-oxo nodes was adapted from a reported procedure from S. Dai et al.[26] A solution of $ZrCl_4$ (1 g, 4.3 mmol) in isopropanol (2 mL) and acetic acid (3 mL) was stirred at 80 °C in a 10 mL Schott flask for 1 h. The resulting white slurry was centrifuged, obtaining $Zr_6O_8H_4(AcO)_{12}$ as a white powder (894.5 mg, 90% yield).

Synthesis of nanosized **Zr-PTPC** crystalline samples. A solution of $Zr_6O_8H_4(AcO)_{12}$ nodes (23 mg, 0.012 mmol, 1 eq.) and PTPC (11 mg, 0.015 mmol, 1.5 eq.) in acetic acid (0.3 mL) and DMF (2 mL) was heated at 120 °C in a 10 mL Schott flask for 48 h. The resulting solid suspension was washed with DMF several time until the yellow color disappeared. Then the solid was washed with water followed by acetone, yielding a nanosized **Zr-PTPC** material as a pale orange solid (16 mg).

Synthesis of microsized **Zr-PTPC** crystalline samples. The procedure for the growth of single crystals of Zr-PTPC was adapted from a general procedure by J. Ma et al.[45] and T. Islamoglu et al.[34] aimed at obtaining crystalline MOF materials. A stock solution A was prepared containing 70 mg of $ZrCl_4$ and 7.60 g of benzoic acid in 10 mL of DMF. A stock solution B was prepared containing 23 mg of PTPC in 10 mL of DMF. A mixture of 1 mL of solution A, 1 mL of solution B, and 20 μL of trifluoroacetic acid was heated in a 10 mL Schott flask applying a 1h heating ramp (1.5 °C min^{-1}) until reaching 120 °C and maintaining this temperature for 48 h. After this time, the sample was let to cool down for 4 h. The resulting red needles were washed with DMF, water, and acetone.

Absorptance spectroscopy measurements. Absorption spectra were measured at room temperature through a synchronous scan using an Edinburgh Instruments FS5 spectrometer equipped with a 150 W CW ozone-free xenon arc lamp, integrating sphere, and a photomultiplier detector (spectral coverage 250–800 nm). The samples were diluted in $BaSO_4$ (1/10 in w/w) and the resulting solid were ground with a mortar to obtain a homogeneous sample. A pure $BaSO_4$ sample was measured as a reference.

Photoluminescence steady-state studies. Steady-state photoluminescence spectra were measured using an Edinburgh Instruments FS5 spectrometer equipped with a 150 W CW ozone-free xenon arc lamp, a sample holder for solids, and a photomultiplier detector (spectral coverage 250–800 nm). The sample holder was placed in a +6° angle to avoid reflections from the solid.

Photoluminescence quantum yield (PLQY) measurements. The PLQY was obtained using an Edinburgh Instruments FS5 Spectrometer equipped with a 150 W CW ozone-free xenon arc lamp, integrated sphere sample chamber, and photomultiplier detector (spectral coverage 250–800 nm). The samples were diluted in $BaSO_4$ (1/10 in w/w) and the resulting solid were ground with a mortar to obtain a homogeneous sample. The PLQY was calculated by using the equation: $\eta_{QE} = I_S/(E_R - E_S)$, in which I_S represents the luminescence emission spectrum of the sample, E_R is the spectrum of the excitation light from the empty integrated sphere (without the sample), and E_S is the excitation spectrum for exciting the sample.

Fluorescence Lifetime Imaging Microscopy (FLIM) measurements. FLIM images were recorded at room temperature using a Leica STELLARIS 8 STED 3X multispectral confocal nano and mesoscopic system, with a 10x dry objective lens. FLIM images were analyzed using Leica LAS-X software. The presented images are of confocal, Fast FLIM, or the graphic representation of lifetimes as a phasor. The reported $\tau_{av.}$ are the amplitude averaged lifetimes, estimated by fitting the fluorescence decay of overall images to tri-exponential functions removing the IRF, and studying the lifetimes over 0.3 ns to get reproducible results without tendency in the residuals and good fitting (χ^2). The error of the measurements is estimated to ± 0.2 ns. Colors in confocal experiments are false-colors. FLIM experiments were recorded within a range of lifetimes/colors that are represented with their corresponding attached bar. Phasor diagrams were also performed by Leica LAS-X software. The details of each experiment are in the corresponding captions.

Supporting Information

Supporting Information is available from the Wiley Online Library or from the author.

Acknowledgements

I.R.-M., J.G.-C., D.R.S.-M., T.T., F.Z., and G.B. acknowledge financial support from the Spanish AEI/MICINN (PID2020-116490GB-I00 and PID2023-151167NB-I00) and the Comunidad de Madrid and the Spanish State through the Recovery, Transformation and Resilience Plan ["Materiales Disruptivos Bidimensionales (2D)" (MAD2D-CM) (UAM1)-MRR Materiales Avanzados (T.T.) and (MAD2D-CM) (UAM2)-MRR Materiales Avanzados (F.Z.)], and the European Union through the Next Generation EU funds. J. G.-C. acknowledges his funding from "Ayudas María Zambrano para la atracción de talento internacional" (CA3/RSUE/ 2021-00243) from the Spanish Government/EU funds at Universidad Autónoma de Madrid, and "Ayudas de atracción de talento de la Comunidad de Madrid 2022" (2022- T1/IND23907) supported by Comunidad de Madrid with EU funds at IMDEA Nanociencia. C. R.-M. acknowledges financial support by the Ramón y Cajal program of the Spanish Ministry of Science and Innovation (Ref. RYC2021-031176-I). J.G.-C, T.T., and G.B. acknowledge support from the "Severo Ochoa" Programme for Centres of Excellence in R&D (MINECO, grant nos. SEV-2016-0686 and CEX2020-001039-S) at IMDEA Nanociencia. I.R.-M. acknowledges the collaboration of Dr. Josefina Perles, Dr. Mario Ramírez, and Dr. Paloma Martínez from the single crystal X-ray diffraction service of UAM (SIdI). J.G.-C acknowledges the collaboration of the advanced light microscopy service of National Centre of Biotechnology (CNB), especially Dr. Gianluca D'Agostino for the FLIM measurements.

Conflict of Interest

The authors declare no conflict of interest.

Author Contributions

I.R.-M. and J.G.-C. contributed equally to this work. We describe contributions to the paper using the CRediT author statement. Investigation: I.R.-M. Synthesis and characterization of $Z_6O_8(AcO)_{12}$ clusters and **Zr-PTPC** MOF, and structure elucidation, analysis of the morphology, and solid-state fluorescence measurements of **Zr-PTPC**; J.G.-C. Ligand synthesis, solution fluorescence and FLIM measurements; C.R.-M. first principles calculations. Conceptualization: I.R.-M. and J.G.-C. Writing – Original draft: I.R.M., J.G.-C., C.R.-M., and G.B. Writing – Review & Editing: I.R.-M., J.G.-C., C.R.-M., D.R.S.-M., T.T., F.Z., and G.B. Project administration: D.R.S.-M., T.T., F.Z., and G.B. Funding acquisition: T.T. and F.Z.

Data Availability Statement

The full data set of the article is available at the repository of the Universidad Autónoma de Madrid at https://repositorio.uam.es/.

Keywords

confocal fluorescence microscopy, fluorescence lifetime imaging microscopy, perylenes, Zr-MOFs

Received: August 9, 2024
Revised: September 18, 2024
Published online: October 15, 2024

[1] R. Katoh, K. Suzuki, A. Furube, M. Kotani, K. Tokumaru, *J. Phys. Chem. C* **2009**, *113*, 2961.
[2] J. T. Markiewicz, F. Wudl, *ACS Appl. Mater. Interfaces* **2015**, *7*, 28063.
[3] A. Nowak-Król, F. Würthner, *Org. Chem. Front.* **2019**, *6*, 1272.
[4] A. Bučinskas, D. Volyniuk, Y. Danyliv, J. V. Grazulevicius, G. Baryshnikov, B. Minaev, K. Ivaniuk, V. Cherpak, P. Stakhira, *RSC Adv.* **2015**, *5*, 78150.
[5] S. V. Dayneko, E. Cieplechowicz, S. S. Bhojgude, J. F. Van Humbeck, M. Pahlevani, G. C. Welch, *Mater. Adv.* **2021**, *2*, 933.
[6] Q. Shi, J. Wu, X. Wu, A. Peng, H. Huang, *Chem. Eur. J.* **2020**, *26*, 12510.
[7] N. Busto, J. García-Calvo, J. V. Cuevas, A. Herrera, J.-L. Mergny, S. Pons, T. Torroba, B. García, *Bioorg. Chem.* **2021**, *108*, 104660.
[8] F. Würthner, *Chem. Commun.* **2004**, 1564.
[9] R. S. Wilson-Kovacs, X. Fang, M. J. Hagemann, H. E. Symons, C. F. Faul, *Chem. Eur. J.* **2022**, *28*, e202103443.
[10] O. M. Yaghi, M. J. Kalmutzki, C. S. Diercks, *Introduction to Reticular Chemistry*, John Wiley & Sons, Hoboken, NJ **2019**.
[11] D. Feng, W.-C. Chung, Z. Wei, Z.-Y. Gu, H.-L. Jiang, Y.-P. Chen, D. J. Darensbourg, H.-C. Zhou, *J. Am. Chem. Soc.* **2013**, *135*, 17105.
[12] R. Chen, Z. Jinfeng, J. Chelora, Y. Xiong, S. V. Kershaw, K. F. Li, P.-K. Lo, K. W. Cheah, A. L. Rogach, J. A. Zapien, C.-S. Lee, *ACS Appl. Mater. Interfaces* **2017**, *9*, 5699.
[13] R. Matheu, E. Gutierrez-Puebla, M. Á. Monge, C. S. Diercks, J. Kang, M. S. Prévot, X. Pei, N. Hanikel, B. Zhang, P. Yang, O. M. Yaghi, *J. Am. Chem. Soc.* **2019**, *141*, 17081.
[14] M. Gutiérrez, C. Martin, K. Kennes, J. Hofkens, M. Van der Auweraer, F. Sánchez, A. Douhal, *Adv. Opt. Mater.* **2018**, *6*, 1701060.
[15] I. del Castillo-Velilla, A. Sousaraei, I. Romero-Muñiz, C. Castillo-Blas, A. S. J. Méndez, F. E. Oropeza, V. A. de la Peña O'Shea, J. Cabanillas-González, A. Mavrandonakis, A. E. Platero-Prats, *Nat. Commun.* **2023**, *14*, 2506.
[16] Y. Shen, J. Ma, S. Li, J. Qian, Q. Li, *Chem. Eng. J.* **2023**, *466*, 143290.
[17] Y. Shen, D. Ma, M. Zhao, J. Qian, Q. Li, *Front. Chem.* **2024**, *12*, 1444036.
[18] I. del Castillo-Velilla, I. Romero-Muñiz, C. Marini, C. Montoro, A. E. Platero-Prats, *Nanoscale* **2024**, *16*, 6627.
[19] J. Dong, D. Zhao, Y. Lu, W.-Y. Sun, *J. Mater. Chem. A.* **2019**, *7*, 22744.
[20] S. Navalón, A. Dhakshinamoorthy, M. Álvaro, B. Ferrer, H. García, *Chem. Rev.* **2023**, *123*, 445.
[21] J.-L. Wang, C. Wang, W. Lin, *ACS Catal.* **2012**, *2*, 2630.
[22] J. E. Mondloch, W. Bury, D. Fairen-Jimenez, S. Kwon, E. J. DeMarco, M. H. Weston, A. A. Sarjeant, S. T. Nguyen, P. C. Stair, R. Q. Snurr, O. K. Farha, J. T. Hupp, *J. Am. Chem. Soc.* **2013**, *135*, 10294.
[23] G. Valente, M. Esteve-Rochina, S. P. C. Alves, J. M. G. Martinho, E. Ortí, J. Calbo, F. A. Almeida Paz, J. Rocha, M. Souto, *Inorg. Chem.* **2023**, *62*, 7834.
[24] G. Valente, M. Esteve-Rochina, A. Paracana, A. Rodríguez-Diéguez, D. Choquesillo-Lazarte, E. Ortí, J. Calbo, M. Ilkaeva, L. Mafra, M. A. Hernández-Rodríguez, J. Rocha, H. Alves, M. Souto, *Mol. Syst. Des. Eng.* **2022**, *7*, 1065.
[25] L. D. Tran, J. Ma, A. G. Wong-Foy, A. J. Matzger, *Chem. Eur. J.* **2016**, *22*, 5509.
[26] S. Dai, C. Simms, I. Dovgaliuk, G. Patriarche, A. Tissot, T. N. Parac-Vogt, C. Serre, *Chem. Mater.* **2021**, *33*, 7057.
[27] I. Romero-Muñiz, C. Romero-Muñiz, I. del Castillo-Velilla, C. Marini, S. Calero, F. Zamora, A. E. Platero-Prats, *ACS Appl. Mater. Interfaces* **2022**, *14*, 27040.
[28] G. Kresse, J. Furthmüller, *Phys. Rev. B.* **1996**, *54*, 11169.
[29] P. E. Blöchl, *Phys. Rev. B.* **1994**, *50*, 17953.
[30] G. Kresse, D. Joubert, *Phys. Rev. B.* **1999**, *59*, 1758.
[31] J. P. Perdew, K. Burke, M. Ernzerhof, *Phys. Rev. Lett.* **1996**, *77*, 3865.
[32] S. Grimme, J. Antony, S. Ehrlich, H. Krieg, *J. Chem. Phys.* **2010**, *132*, 154104.
[33] N. Planas, J. E. Mondloch, S. Tussupbayev, J. Borycz, L. Gagliardi, J. T. Hupp, O. K. Farha, C. J. Cramer, *J. Phys. Chem. Lett.* **2014**, *5*, 3716.
[34] T. Islamoglu, K.-i. Otake, P. Li, C. T. Buru, A. W. Peters, I. Akpinar, S. J. Garibay, O. K. Farha, *CrystEngComm.* **2018**, *20*, 5913.
[35] B. Gibbons, E. C. Bartlett, M. Cai, X. Yang, E. M. Johnson, A. J. Morris, *Inorg. Chem.* **2021**, *60*, 16378.
[36] T. Seko, K. Ogura, Y. Kawakami, H. Sugino, H. Toyotama, J. Tanaka, *Chem. Phys. Lett.* **1998**, *291*, 438.
[37] W. Ni, L. Sun, G. G. Gurzadyan, *Sci. Rep.* **2021**, *11*, 5220.
[38] N. J. Hestand, F. C. Spano, *Chem. Rev.* **2018**, *118*, 7069.
[39] K. Sato, R. Katoh, *Chem. Phys. Lett.* **2019**, *730*, 312.
[40] E. Caballero-Mancebo, B. Cohen, S. Smolders, D. E. De Vos, A. Douhal, *Adv. Sci.* **2019**, *6*, 1901020.
[41] J. Yu, J. Park, A. Van Wyk, G. Rumbles, P. Deria, *J. Am. Chem. Soc.* **2018**, *140*, 10488.
[42] P. Deria, J. Yu, T. Smith, R. P. Balaraman, *J. Am. Chem. Soc.* **2017**, *139*, 5973.
[43] Z. Zhang, W. Ni, L. Ma, L. Sun, G. G. Gurzadyan, *J. Phys. Chem. C.* **2022**, *126*, 396.
[44] C. Qiu, G. J. Blanchard, *J. Phys. Chem. B.* **2014**, *118*, 10525.
[45] J. Ma, L. D. Tran, A. J. Matzger, *Cryst. Growth Des.* **2016**, *16*, 4148.